Journal of Physical Chemistry C

Manuscript ID: jp-2023-01160a

Comparative studies on [B(HFIP)$_4$]-Based Electrolytes with Mono- and Divalent Cations

Toshihiko Mandai[1,2*], Hiroko Naya[1], and Hyuma Masu[3]

[1]Center for Green Research on Energy and Environmental Materials, National Institute for Materials Science (NIMS), 1-1 Namiki, Tsukuba, Ibaraki 305-0044, Japan

[2]Center for Advanced Battery Collaboration, National Institute for Materials Science (NIMS), 1-1 Namiki, Tsukuba, Ibaraki 305-0044, Japan

[3]Center for Analytical Instrumentation, Chiba University, 1-33 Yayoi-cho, Inage-ku, Chiba 263-8522, Japan

*Contact

Mail: MANDAI.Toshihiko@nims.go.jp TEL: +81-29-860-4464

Abstract

The development of electrolyte materials that are compatible with reductive metals is an urgent requirement for realizing high-energy-density rechargeable batteries utilizing metallic negative electrodes. Due to successive changes and regeneration of the morphology and fresh metals, respectively, upon repeated cycling of the metallic electrodes, the electrolytes should possess sufficient (electro)chemical stabilities against such electrodes. Weakly coordinating anion (WCA)-based electrolytes, which were first proposed for lithium-based battery applications in 1995, have attracted significant attention, especially in recent years, owing to their successful application in magnesium and calcium metal batteries. Inspired by these studies, WCA-based electrolytes have been re-imported into lithium- and sodium-ion battery chemistry. In this study, we conducted comprehensive comparative studies on the representative WCA-based electrolytes incorporating tetrakis(hexafluoro-iso-propoxyl)borate ($[B(HFIP)_4]^-$) anions as a model system to understand the effect of valency of paired cation species on transport properties and electrochemical characteristics. As revealed by X-ray crystallography, the monovalent lithium and sodium salts were obtained as adducts, where the anion participated in cation coordination along with a single solvent molecule, whereas divalent magnesium, calcium, and zinc salts formed fully isolated solvates with the divalent cations being coordinated by solvents alone. Such valency-dependent differences in the dissociation states would affect the solution properties, as the divalent electrolytes exhibited greater conductivities than their monovalent counterparts, even though the same number of charged species were present in the respective solutions. The electrochemical metal deposition/dissolution studies combined with morphological and subsequent elemental analysis on the deposits suggested the specific favorable combination of magnesium cations and $[B(HFIP)_4]^-$ anion in ethereal solutions. The modest surface reactivity of the deposited macrocrystalline magnesium, moderate reductive

nature of the magnesium metal, and well-balanced mutual interactions among the components may have jointly contributed to such outstanding performance.

Keywords: borate, divalent metal, electrolyte, monovalent metal, stability

Introduction

Modern industrial revolution has induced vast technological innovations and improved human life. These innovations have simultaneously led to severe environmental pollution and the consumption of natural resources. To address such environmental concerns and realize a sustainable society in the future, highly efficient energy harvesting and storage technologies based on renewable energy sources are urgently required. Rechargeable batteries that incorporate bulk metals as the negative electrode active material are promising energy storage technologies for responding to these demands. The replacement of graphite in conventional lithium-ion batteries with bulk metals as negative electrodes can considerably enhance the energy densities of batteries owing to the substantially large volumetric and gravimetric capacities of bulk metals.[1,2] Significant research efforts have been made to achieve high-energy-density rechargeable batteries with metallic negative electrodes, and many potential techniques along the fundamental/mechanistic understanding have been developed;[3–12] however, the development of suitable electrolyte materials remains a bottleneck.

Because electrochemical metal deposition/dissolution reactions are fundamental electrochemical processes that occur at metal negative electrodes during the charge/discharge of batteries, electrolytes that allow these reactions to occur reversibly with sufficiently high efficiencies are required. Although conventional carbonate-based electrolytes support the relatively reversible electrochemical reactions of monovalent lithium and sodium metals,[13–16] those mimetics are generally incompatible with divalent Mg and Ca metals; hence, specific electrolytes for divalent metals need to be explored.[17,18] Weakly coordinating anion (WCA)-based electrolytes are an innovative class, especially for multivalent metal batteries. The concept of WCAs has been proposed to improve the ionic conductivity and thermal stability of the electrolytes for lithium-based batteries since at least 1995.[19–27] Among the substantially large variety of WCAs, the quaternary borates and aluminates bearing fluorinated-alkoxide

functional groups, such as tetrakis(hexafluoro-iso-propoxyl)borate ($[B(HFIP)_4]^-$), tetrakis(hexafluoro-iso-propoxyl)aluminate ($[Al(HFIP)_4]^-$), and tetrakis(perfluoro-tert-butoxy)aluminate ($[Al(PFTB)_4]^-$), are promising owing to their excellent dissociativity and sufficient cathodic/anodic stability. The electrolytes based on these supporting salts indeed support reversible metal deposition/dissolution cycling with remarkable efficiencies and substantially contribute to paving the way for multivalent battery materializations.[28–37] Inspired by these success stories of WCA-based electrolytes in multivalent battery fields, the concept has recently been reimported in lithium and sodium battery chemistry, especially those utilizing metallic negative electrodes combined with high-performance positive electrodes.[38–41] Combined theoretical and experimental studies have also been conducted to understand the origin of such characteristics of WCAs, especially in magnesium battery electrolytes.[32, 42–44]

In this study, we conducted comprehensive comparative studies on the representative WCA-based electrolytes incorporating $[B(HFIP)_4]^-$ anions to understand the effect of valency of paired cation species on transport properties and electrochemical characteristics. Based on the analysis of the molecular structures of the salts combined with the transport and electrochemical properties of the electrolyte solutions, the paired cation-independent universal and cation-dependent unique characteristics of $[B(HFIP)_4]^-$ are discussed. Instead of a simple electrode potential of each metal, a rather complicated balance of the mutual interactions among metal cations, $[B(HFIP)_4]^-$ anions, and ethereal solvents was found to predominate the compatibility of the electrolytes with metallic negative electrodes.

Methods

Materials. The electrolyte salts-based on the $[B(HFIP)_4]^-$ anion paired with Li, Na, Mg, Ca, or Zn ions were synthesized according to the reported procedures.[29,32,36,45] $Li[B(HFIP)_4]$ and

$Na[B(HFIP)_4]$ were obtained through a simple alcoholysis reaction of hexafluoro-iso-propanol (HFIP-H) by the corresponding alkali metal borohydride. Divalent salts were synthesized by transmetalation between $M(II)(HFIP)_2$ and $B(HFIP)_3$. The chemical structures of the synthesized salts were identified by ^1H NMR spectroscopy, followed by absolute structure determination by X-ray crystallography. Because of the low crystallinity of the divalent salts, structural refinement using the least-squares method did not converge. The compositions and approximate structures of the obtained $Mg[B(HFIP)_4]_2$ and $Ca[B(HFIP)_4]_2$ salts were confirmed to be the same as those reported from the NMR spectra. Reference monovalent and divalent salts incorporating the bis(trifluoromethanesulfonyl)amide ($[TFSA]^-$) anions were purchased from TCI (Li and Na), Kishida Chemicals (Mg and Ca), and Solvionic (Zn). All salts were dried under high vacuum at 45 °C for $[B(HFIP)_4]$- and at 120 °C for [TFSA]-based salts for 3 days prior to use. A series of electrolyte solutions were prepared by dissolving predetermined amounts of the salts in monoglyme (G1) and diglyme (G2), and the solutions were vigorously stirred at 30 °C overnight in an Ar-filled glovebox (O_2, H_2O < 1 ppm, UNICO). The salt concentrations were determined to be 0.25 and 0.5 mol dm^{-3} for divalent and monovalent systems, respectively, to fix the resulting net (positive and negative) charge concentration to be 1 mol dm^{-3}. The water content of the prepared electrolytes was measured to be < 50 ppm using Karl Fischer titration.

Crystallography: X-ray crystallography was performed on single crystals of $Li[B(HFIP)_4]$, $Na[B(HFIP)_4]$, $Ca[B(HFIP)_4]_2$, and $Zn[B(HFIP)_4]_2$ obtained by recrystallization from the concentrated G1 solutions. All measurements were made on a Rigaku XtaLab Pro HPC diffractometer with Mo-Kα radiation (λ = 0.71073 Å) or Bruker ApexII Ultra CCD diffractometer with Cu-Kα radiation (λ = 1.54178 Å). Data were collected at low temperatures (173 or 153 K) under a steady flow of nitrogen gas. The reflection data were collected and processed using CrysAlisPro (version 1.171.39.46e; Rigaku Corporation) or Bruker Apex3

(Bruker AXS, 2006), followed by the application of an empirical absorption correction technique. The structures were solved using the direct method of SHELXT and refined using full-matrix least-squares in an anisotropic approximation for nonhydrogen atoms using SHELXL. All the hydrogen atoms were placed in ideal positions and refined using an isotropic riding model. The crystallographic information file (cif) was deposited in the Cambridge Structure Database (CSD) as CCDC 2243156 for $Li[B(HFIP)_4]$. Because the structure of $Na[B(HFIP)_4]$ is identical to the reported one,[45] the cif was not deposited. The crystallographic data of the $Ca[B(HFIP)_4]_2$ and $Zn[B(HFIP)_4]_2$ crystals were also not deposited because of the absence of good-quality refinement models. Detailed crystallographic data and solved structures are summarized in Table S1 and Figures S1 ($Li[B(HFIP)_4]$) and S2 ($Na[B(HFIP)_4]$).

Transport properties. Ionic conductivity, liquid density, and viscosity of the electrolytes were evaluated in this study. Ionic conductivities were measured using the complex impedance method with an impedance analyzer (VMP3, Biologic). The liquid density and viscosity were measured using a kinematic viscometer (SVM3001, Anton Paar GmbH). A temperature range of 20−50 °C was adopted for all the measurements. All standard deviations of the experimental values were within 3% of the average.

Electrochemistry. The electrochemical metal deposition-dissolution activities of a series of mono-and divalent $[B(HFIP)_4]$-based electrolytes were assessed by cyclic voltammetry (CV) using a typical three-electrode beaker-type cell. Copper disks wrapped with poly-ether-ether ketone resin (φ3 mm, BAS) served as the working electrodes, while pieces of the corresponding metals were used as both counter and reference electrodes. The CV was performed at a scan rate of 10 mV s^{-1} and 30 °C. The deposits were obtained by galvanostatic polarization at a current density of 2 mA cm^{-2} at 30 °C. Electrochemical measurements were conducted using

electrochemical analyzers HSV-110 (Hokuto–Denko Corporation) and VMP3 (Biologic) located in an Ar-filled glovebox.

Vibrational Analysis. The coordination states of mono- and divalent cations in solutions were examined by comparing the Raman spectra of the parent salts and their solutions. The spectra were collected with a Nicolet iS50R FT-Raman spectrometer (Themo Scientific) equipped with a 1064-nm laser at a resolution of 1 cm^{-1}. The single crystals of the salts and their G1 solutions were hermetically sealed in a glass tube in an Ar-filled glovebox, then subjected to the spectrometer located in a dry room to avoid any exposure to moisture. The spectra were all calibrated by the polypropylene standard.

Morphological and Chemical Analysis. The electrodeposited metals were observed by scanning electron microscopy (SEM; JSM-7800F, JEOL) and characterized by energy-dispersive X-ray (EDX) spectroscopy and X-ray photoelectron spectroscopy (XPS; VersaProbe II, ULVAC-PHI, Japan). All the samples were washed with anhydrous ethylene glycol dimethyl ether to remove any residual electrolyte, dried under high vacuum at ambient temperature, placed in an airtight chamber, and transferred for SEM–EDX and XPS analysis without any exposure to air. XPS measurements were performed with an Al Kα X-ray source under a base pressure of 6.7×10^{-8} Pa. The binding energy of the obtained spectra was calibrated using the C 1s peak from sp2-hybridized carbon at 284.5 eV as a reference. Note that, the XPS spectra of the Zn deposits were not acquired due to the relatively high sublimation nature of Zn compounds.[46]

Results and Discussion

Synthesis and structural analysis of [B(HFIP)$_4$] salts: Monovalent [B(HFIP)$_4$] salts were synthesized by simple alcoholysis of HFIP-H with precursor borohydride salts according to

previously reported procedures (Eq. 1).[38,45] The final products were obtained as a white powder after vacuum heating of the concentrated G1 solutions at 45 °C for 2 days, and their chemical compositions were identified as an adduct of M(I)[B(HFIP)$_4$] with a single solvent molecule (G1), irrespective of the alkali metal ions, by NMR (Figure S3a) and X-ray crystallography (Figure 1). In contrast, the corresponding divalent salts were synthesized by the transmetalation between M(II)(HFIP)$_2$ and B(HFIP)$_3$ to avoid undetectable, unavoidable contamination from the starting reagents or the precursor borohydride salts (Eq. 2). As the difference in Lewis acidity or affinity of the transferred functional groups against two different ions is usually the driving force during transmetalation reactions, it is advantageous to use mono- and divalent cations for the synthesis of alkoxyborate salts, especially when the corresponding borohydride salts, such as Zn(BH$_4$)$_2$, are not commercially available. The divalent salts were isolated as colorless crystals from the concentrated solvent G1 solution, followed by vacuum heating at 45 °C for 3 days. In contrast to those of the monovalent salts, the chemical compositions of the divalent salts identified by NMR were cation-dependent. The integral intensities of the peaks assignable to each HFIP group and remaining G1 molecules suggested formation of the Mg[B(HFIP)$_4$]$_2$·3G1, Ca[B(HFIP)$_4$]$_2$·4G1, and Zn[B(HFIP)$_4$]$_2$·3G1 adducts/solvates (Figure S3b) and confirmed comparable composition between the Mg and Ca salts as reported previously.[28,29,35,36]

$$\mathrm{M(I)BH_4 + 4HFIP\text{-}H \xrightarrow{G1,\ r.t.,\ 24h} M[B(HFIP)_4] + H_2} \qquad (1)$$

$$\mathrm{M(II)(HFIP)_2 + 2B(HFIP)_3 \xrightarrow{G1,\ r.t.,\ 48h} M(II)[B(HFIP)_4]_2} \qquad (2)$$

The molecular structures of the mono- and divalent [B(HFIP)$_4$]$^-$ salts are shown in Figure 1. Owing to the substantially low crystallinity of the divalent salts, the structural refinement did not converge well (R_1 > 0.150 and wR_2 > 0.450). Therefore, refinement models cannot be used to discuss the structural parameters. The obtained structure, however, ensures

the relative atomic coordinates and chemical composition and can provide significant insights into the solvation structures of divalent salts. Indeed, our refinement model of $Ca[B(HFIP)_4]_2 \cdot 4G1$ seems identical to those reported one with respect to the unit cell parameters and chemical composition.[35,36] The structure of $Mg[B(HFIP)_4]_2 \cdot 3G1$ was reproduced using the data deposited in the Cambridge Crystal Structure Data Center with accession number CCDC 1537493 because of the extremely poor-quality refinement model obtained in our study. For the monovalent $[B(HFIP)_4]^-$ salts, a single solvent G1 was involved in the molecular unit irrespective of the cation species, as confirmed in the ^1H NMR spectra (Figure S3a). However, the coordination state of the $[B(HFIP)_4]^-$ anion was distinct. For $Li[B(HFIP)_4] \cdot G1$, Li^+ ion was coordinated by two oxygen atoms from a single $[B(HFIP)_4]^-$ in bidentate form in addition to the bidentate coordination from a G1 molecule, resulting in the formation of the tetra-coordinated complex. In contrast, Na^+ ion was coordinated by a single $[B(HFIP)_4]^-$ anion in tetradentate form where two oxygen atoms in the two individual HFIP groups and two additional fluorine atoms in the two individual CF_3 branches (one from the same and another from a different HFIP group for the O-coordination) participated in coordination, thereby forming the hexa-coordinated complex for $Na[B(HFIP)_4] \cdot G1$. This difference in the coordination mode may arise from the preferential coordination numbers of Li^+ (4–5) and Na^+ (5–6) in the solid state. The coordination state of the anion for the divalent $[B(HFIP)_4]^-$ salts was distinct from that for the monovalent counterparts. The cation species and $[B(HFIP)_4]^-$ were completely isolated and the cations were stabilized only by G1 coordination. The preferential coordination numbers of Mg^{2+} (6–7), Ca^{2+} (6–8), and Zn^{2+} (4–6) in the solid state were responsible for the resulting number of G1 molecules in the crystal structure.

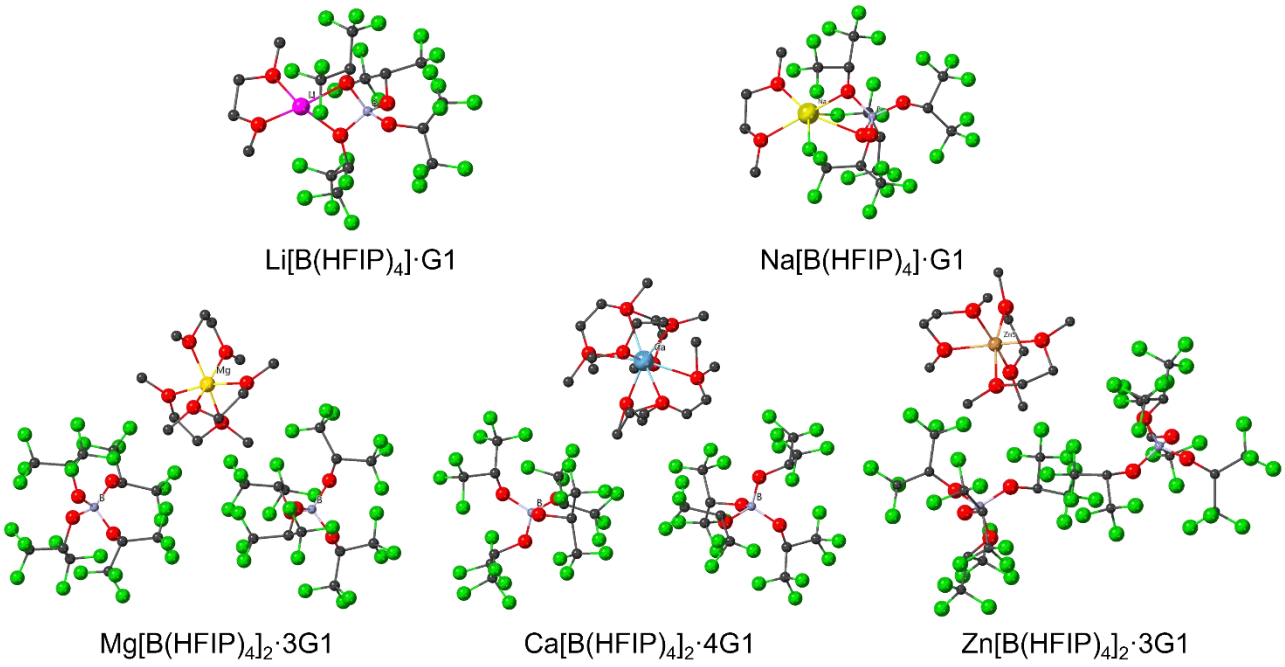

Figure 1. Molecular structures of $Li[B(HFIP)_4]\cdot G1$, $Na[B(HFIP)_4]\cdot G1$, $Mg[B(HFIP)_4]_2\cdot 3G1$, $Ca[B(HFIP)_4]_2\cdot 4G1$, and $Zn[B(HFIP)_4]_2\cdot 3G1$ crystals, presented as the ball and stick models. Hydrogen and disordered atoms are omitted for clarity. The structure of the Mg solvate was reproduced from CCDC 1537493.

The coordinating ability of the studied $[B(HFIP)_4]^-$ anion is known to be remarkably low owing to the structural bulkiness and electron-withdrawing nature of the HFIP groups.[28,42,43] Based on the solvate category according to the coordination state of anions, the monovalent salts belong to the contact ion-pair (CIP) where counter anions participate in coordination, while the divalent salts are categorized according to the solvent-separated ion-pair (SSIP) where the cation-anion pair is isolated/separated by solvent(s). The large contributions of the induction interactions to cation-glyme complex formation can account for the difference in the coordination state of the anion. Because of the strong electric field of the metal ions, the electronic states of the ether oxygen atoms in the surrounding glyme molecules were highly polarized. The valency of metal ions and distances between metal ions and oxygen atoms have a strong impact on the level of such polarization, and substantially large

stabilization energy can be gained upon coordination of glymes to multivalent ions.[47,48] Indeed, the formation energies for Mg^{2+}-glyme complexes (e.g., −157.6 and −288.3 kcal mol^{-1} for G1 and G4, respectively) are estimated to be approximately 2.5 times larger compared to those of the corresponding Li^{+}-glyme complexes (e.g., −61.0 and −107.7 kcal mol^{-1} for G1 and G4, respectively).[47,48] The formation energies for Ca^{2+}-glyme complexes are still larger than those for the Li^{+}-glyme complexes despite the less charge density of Ca^{2+} compared to that of Mg^{2+}.[48] Although the stabilization energies for Zn^{2+}-glyme complex formation are unclear, the comparable ionic radii for the hexa-coordinate states and the same valency of Mg^{2+} and Zn^{2+} support the formation of the SSIP-type solvate for $Zn[B(HFIP)_4]_2$ with G1 molecules. Moreover, recent molecular dynamic simulation studies have suggested the partial decomposition of $[B(HFIP)_4]^{-}$ upon ion pair formation with Mg^{2+}.[42–44] Such structural instability during ion pair formation further supports the formation of SSIP-type solvate structures for divalent salts. However, in the case of monovalent salts, the contribution of glyme coordination to complex structure formation is not very large. To gain sufficient structural stabilization, the distorted tetrahedral $[B(HFIP)_4]^{-}$ anion have to participate in the coordination for Li^{+} and Na^{+}. Similar structural features have also been observed in weakly coordinating anion-based monovalent solvates.[24,39]

All the synthesized salts were obtained as solvates with G1 molecule(s). All attempts to isolate the non-solvated salts by vacuum heating at elevated temperature failed irrespective of the cation species, as the color of the powders apparently turned brownish at high temperatures, e.g., 80 °C, indicative of undesired thermal decomposition. These results are consistent with those of previous studies.[39,45] Because the remaining solvent molecule(s) can significantly affect the resulting transport properties, electrolyte solutions of the $[B(HFIP)_4]$-based salts were prepared by dissolving the salts in G1 solvents and investigated for their transport and electrochemical characteristics to avoid ambiguous effects originating from the

mutual interactions of dual solvents. Hereafter, the electrolyte solutions are denoted as M(I or II)[B(HFIP)$_4$]$_n$/G1 (n = 1 or 2).

Transport properties: The transport properties of charge carriers are significant determining factors of battery performance. The ionic conductivities and solution viscosities of 0.5 mol dm^{-3} M(I)[B(HFIP)$_4$]/G1 and 0.25 mol dm^{-3} M(II)[B(HFIP)$_4$]$_2$/G1 measured at 30 °C are summarized in Figure 2. For the ethereal solutions of divalent M(II)[Z(HFIP)$_4$]$_2$ (Z = B or Al), the conductivity maxima occurs at around 0.25–0.4 mol dm^{-3} irrespective of the cation species, the structure of ethereal solvents, and temperature, possibly owing to the trade-off between the change in the number of charge carriers and solution viscosities with the salt concentration.[32] In contrast, the solubility limitation of Li[B(HFIP)$_4$] is laid around 0.6 mol dm^{-3} at 30 °C. According to these experimental facts for weakly-coordinating anion-based electrolytes, the net (positive and negative) charge concentration of the studied electrolyte solutions was fixed at 1 mol dm^{-3} in this study. The effects of the measured temperature and electrolyte concentration on ionic conductivity are shown in Figure S4.

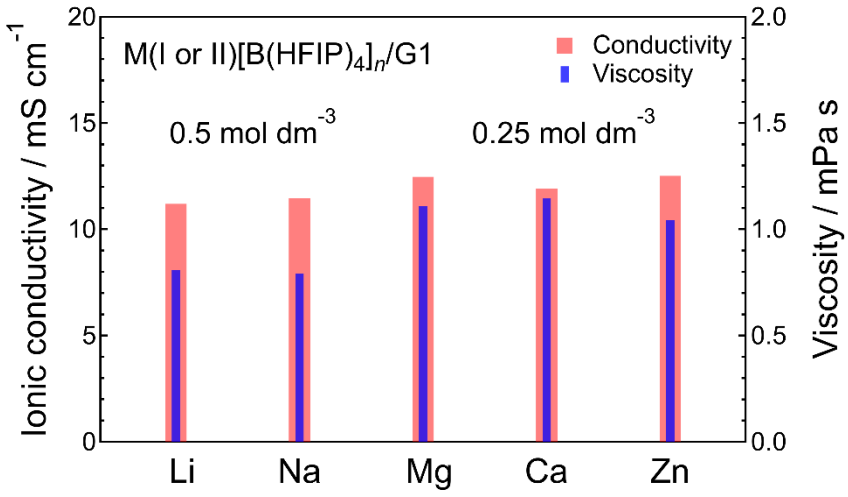

Figure 2. Ionic conductivities and viscosities of 0.5 mol dm^{-3} M(I)[B(HFIP)$_4$]/G1 and 0.25 mol dm^{-3} M(II)[B(HFIP)$_4$]$_2$/G1 measured at 30 °C.

Figure 2 illustrates the effect of the valence of the cation species on the transport properties. The viscosities of the monovalent salt-based electrolytes were apparently lower than those of the divalent salt-based electrolytes, whereas the ionic conductivities were comparable among the electrolytes irrespective of the cation species. In general, low-viscosity solutions can deliver charge carriers present in the solutions rapidly; therefore, greater conductivity would be observed with decreasing solution viscosities for the same charge carrier concentration. This observation suggests that the number of charge carriers is greater in divalent salt-based electrolytes than in monovalent-based electrolytes. In other words, the divalent $[B(HFIP)_4]^-$ salts are prone to be well dissociated in solutions even though the divalent metal cations would attract counter anions more tightly than the monovalent metal cations. One of the representative, conventional electrolyte solutions based on the modestly coordinated $[TFSA]^-$ anions indeed showed rather predictable results (Figure S5), where substantially lower conductivities were observed for the divalent systems than those for the monovalent counterparts. Similar trends as observed in the [TFSA]-based solutions have also been reported for solutions incorporating different monovalent anions such as PF_6^- or $CF_3SO_3^-$,[49–52] indicating characteristic transport behavior of the $[B(HFIP)_4]$-based systems. Notably, $[TFSA]^-$ based electrolytes were prepared by dissolving the salts not in G1 but in G2, because the G1 solutions of the divalent $[TFSA]^-$ salts resulted in liquid-liquid phase separation in the broad concentration range while clear solutions can be obtained for the monovalent $[TFSA]^-$ electrolytes. Such peculiar phase behavior for $Mg[TFSA]_2$/G1 has extensively been studied by Salama et al., and is suggested to be induced by formation of a kind of suprastructure that consists of an exceptionally stable $Mg[TFSA]_2 \cdot 3G1$ complex surrounded by certain number of G1 molecules in a long-range order.[53] Owing to the similar physicochemical nature among divalent Mg^{2+}, Ca^{2+} and Zn^{2+} ions, the miscibility gap phenomena here observed in the $Zn[TFSA]_2$/G1 and $Ca[TFSA]_2$/G1 solutions can also be explained by a similar manner. This undesired situation disables the

quantitative comparison of the experimental values among the $[B(HFIP)_4]$- and [TFSA]-based electrolytes. However, a qualitative discussion is still reasonable because of the comparable coordination/polarization nature of different glymes.[48,54,55]

To gain further understanding of the dissociation states, the molar conductivities (Λ) were plotted against the reciprocal of the viscosity (η). Such Walden plots are often referred to as useful measures of salt dissociation in electrolyte solutions. The dotted line with a slope of unity shown in Figure 3 indicates the ideal line where the charged species are completely dissociated and contribute to ion conduction. As predicted from the experimental results, the plots of $M(II)[B(HFIP)_4]_2$/G1 were closer to the ideal line than those of $M(I)[B(HFIP)_4]$/G1, whereas the opposite trend was discernible for the [TFSA]-based solutions (Figure 3). These results further highlight the well-dissociated states of the former divalent electrolyte solutions. The large contribution of induction interactions by the solvent G1 coordination to the structural stability and the substantially weak coordinating nature of the $[B(HFIP)_4]^-$ anion are, again, responsible for this result.

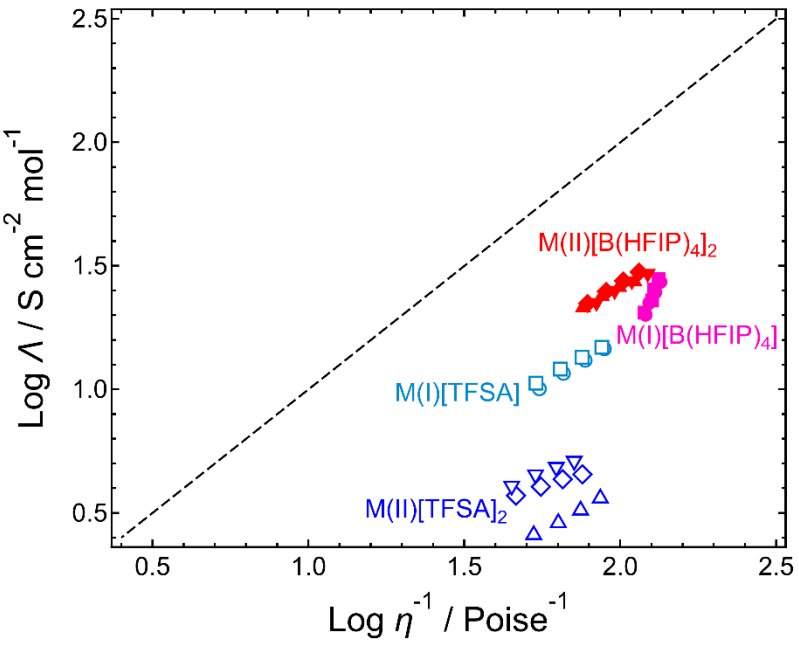

Figure 3. Walden plot for 0.5 mol dm^{-3} M(I)[B(HFIP)$_4$]/G1 and 0.25 mol dm^{-3} M(II)[B(HFIP)$_4$]$_2$/G1 with an ideal line. The points for the corresponding [TFSA]-based solutions of G2 are also included.

The slope of the Walden plot indicates the susceptibility of the dissociation states of the solutions to temperature. The slopes of the plots for M(II)[B(HFIP)$_4$]$_2$/G1, M(I)[TFSA]/G2, and M(II)[TFSA]$_2$/G2 are comparable and almost parallel to the ideal line, suggesting that the salt dissociation state in these solutions is less temperature-dependent. In contrast, the corresponding slope for M(I)[B(HFIP)$_4$] was rather steep. This observation indicates that the salt dissociated considerably with increasing temperature for M(I)[B(HFIP)$_4$]. As evidenced by their molecular structures and the relatively lower dissociativity of M(I)[B(HFIP)$_4$]/G1 than that of M(II)[B(HFIP)$_4$]$_2$/G1, the cation-anion complexes of M^+-[B(HFIP)$_4$]$^-$ with G1 coordination were also present to some extent in the solution. Such cation-anion binding is perturbed at elevated temperatures, possibly resulting in well-dissociated solution states.

Electrochemical characteristics The electrochemical metal deposition-dissolution behavior of a series of electrolyte solutions was assessed by CV. Figure 4 shows the CV profiles of the copper working electrodes recorded in the M(I)[B(HFIP)$_4$]/G1 and M(II)[B(HFIP)$_4$]$_2$/G1 electrolytes. The potential ranges of different electrochemistries were normalized to the potential of a standard hydrogen electrode (SHE). All the studied electrolytes supported the electrochemical deposition-dissolution of each corresponding metal, while the efficiencies and overpotentials strongly depended on the metals to be processed. The overpotentials defined at the potentials where 0.1 mA cm^{-2} of current densities those attributable to deposition ($\eta_{\mathrm{deposition}}$) or dissolution ($\eta_{\mathrm{dissolution}}$) were observed, and the corresponding Coulombic efficiencies estimated from the charge passed during deposition-dissolution processes are summarized in Table 1. As shown in Figure 4 and Table 1, the monovalent salt-based solutions showed

favorable electrochemical activities, as the deposition and dissolution took place with relatively high efficiency and remarkably small overpotential, irrespective of the metal species. The cycling behavior of the present Na-based electrolytes seems better than that of the reported electrolyte of 1 mol dm^{-3} $Na[B(HFIP)_4]$·G1/EC-DEC (EC: ethylene carbonate; DEC: diethyl carbonate),[39] suggesting the superior reduction stability of ether solvents. In contrast to monovalent systems, divalent salt-based electrolytes require large overpotentials, especially for the deposition processes, and their corresponding efficiency strongly depends on the metal species. In particular, for multivalent electrolytes, owing to the activation barrier for desolvation and solvation, the processes at the [electrode | electrolyte] interfaces are regarded as the dominant rate-determining processes for deposition and dissolution, respectively.[32,56,57] The remarkably strong solvation of divalent metal ions hampers facile desolvation during deposition, which would be beneficial for dissolution. The observed overpotentials for the Mg- and Ca-based electrolytes support this hypothesis. Unexpectedly, Zn-based electrolytes showed exceptionally large overpotential for dissolution despite similar charge densities between Zn^{2+} (0.74 Å) and Mg^{2+} (0.76 Å). A similar non-trivial observation has also been reported for Zn-based non-aqueous ethereal electrolytes incorporating different anion species, such as PF_6^-, BF_4^-, $CF_3SO_3^-$, and $[TFSA]^-$.[58] In contrast, Zn-based non-ethereal electrolytes exhibited favorable electrochemical deposition-dissolution characteristics, irrespective of the anion and solvent choices (Figure S6).[37,58] These universal observations strongly suggest the nontrivial oxyphilic nature of Zn^{2+} with respect to ether oxygen atoms. Moreover, Zn^{2+} ions prefer four or six coordinations. This preference can result in complex solution states. The unexpectedly low Coulombic efficiency of the Zn-based electrolytes, despite the substantially inferior reductive nature of Zn metal, supports the existence of somewhat different (electro)chemistries behind the electrochemical Zn deposition-dissolution processes in ethereal electrolytes.

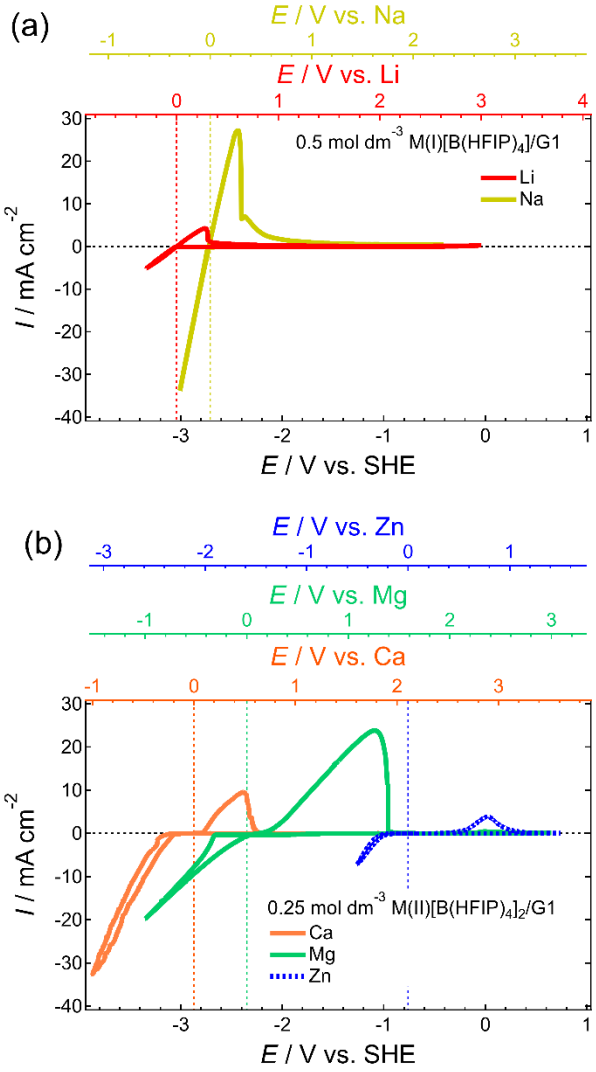

Figure 4. CV profiles of copper working electrodes recorded in (a) 0.5 mol dm^{-3} M(I)[B(HFIP)$_4$]/G1 and (b) 0.25 mol dm^{-3} M(II)[B(HFIP)$_4$]$_2$/G1 electrolytes measured at a scan rate of 10 mV s^{-1} at 30 °C.

Table 1. Overpotential (η) for electrochemical metal deposition and dissolution processes and corresponding Coulombic efficiencies estimated from the CV profiles shown in Figure 4.

	Monovalent cations		Divalent cations		
	Li	Na	Ca	Mg	Zn
$\eta_{deposition}$ / V	0.017	0.022	0.258	0.286	0.208
$\eta_{dissolution}$ / V	0.001	0.016	0.087	0.093	0.337

Efficiency / %	89.8	78.4	12.9	93.7	73.7

The Coulombic efficiencies for metal deposition-dissolution reflect the reductive nature of each metal and the supposed solvation (or ion association) states. Basically, the reductive stability of the $[B(HFIP)_4]^-$ is calculated to be approximately −4 V *vs*. SHE, with the value slightly depending on the calculation model used.[29,42,43] This value implies that $[B(HFIP)_4]^-$ would potentially be stable against reductive metals including lithium. This favorable situation drastically changes upon ion-pair formation because the electric field of small metal ions strongly polarizes the electronic states of the interacting compounds. As described before, such solvation effect becomes prominent in case of multivalent ion systems.[42] The cathodic limits of $[B(HFIP)_4]^-$ would indeed shift to positive side by approximately +3 V upon ion-pair formation with Mg^{2+} and Ca^{2+},[43] and such contacted $[B(HFIP)_4]^-$ anions are no longer stable even against moderately reductive magnesium. For the monovalent $[B(HFIP)_4]^-$ based electrolytes, inferior efficiency was confirmed for the Na-based electrolytes compared to the Li-based electrolytes. As the reductive nature of Na is weaker than that of Li based on their electrode potentials, the difference in associativity of $[B(HFIP)_4]^-$ for Na^+ and Li^+ might have largely contributed to the obtained results. The molecular structure shown in Figure 1 indicate direct contact of both O and F atoms of $[B(HFIP)_4]^-$ to Na^+. An anion decomposition mechanism driven by F abstraction has been proposed based on a recent molecular dynamic simulation study on the $Mg[B(HFIP)_4]_2$-based electrolytes.[42] Although the association states of $[B(HFIP)_4]$ in the bulk $Na[B(HFIP)_4]$/G1 electrolyte solutions are unclear due to the featureless Raman spectra of $M(I)[B(HFIP)_4]$ and $M(II)[B(HFIP)_4]_2$ in the solid and solution states (Figure S7), the agglomeration of charged species at the electric double layer generated during electrochemical processes and resulting direct interaction of F atoms and Na^+ ions presumably led to undesired decomposition of $[B(HFIP)_4]^-$ anion. Elemental analysis of the deposits

obtained from $Na[B(HFIP)_4]$/G1 also supported a relatively large contribution from anion decomposition during Na deposition (vide infra).

In divalent systems, the efficiency of Ca-based electrolytes is substantially low. This was due to the extremely reductive nature of the deposited calcium. As evidenced by the Ellingham diagram,[59] calcium metal is the strongest reducing agent, and most compounds are reduced upon reacting with calcium. Moreover, the geometrical size of the deposits is generally small; hence, the surface area should be significantly larger than that of bulk metals. Owing to the large surface area and the resulting extreme reactivity of the deposited microcrystalline calcium, the G1 molecules polarized upon solvation to Ca^{2+} were readily decomposed during the deposition processes. It should be noted that the present efficiency is exceptionally low compared to the reported values, in the range of 50–80%.[35,36,60] This large difference may arise from the difference in experimental setups and measurement conditions. As expected from the polarization behavior of the $Zn[B(HFIP)_4]_2$/G1 electrolyte shown in Figure 4, the corresponding efficiency is substantially lower than that of its Mg-based counterpart. The sizes and morphologies of the deposits may explain these results. Under the same galvanostatic condition, submicron-sized hexagonal microcrystals were obtained from $Zn[B(HFIP)_4]_2$/G1 while substantially larger particles (> 10 μm) were observed for the case of $Mg[B(HFIP)_4]_2$/G1 (Figure 5). Such submicron-sized microcrystal deposition is supported by the corresponding polarization curves, as a large overpotential is necessary for Zn deposition, which can lead to a nucleation-dominant deposition mode. Additionally, the orientation of Zn deposits is prone to be random under standard conditions.[61] The reaction with such freshly plated, randomly stacked microcrystalline zinc metals might have led to the unexpectedly lower efficiency of the $Zn[B(HFIP)_4]_2$/G1 electrolyte.

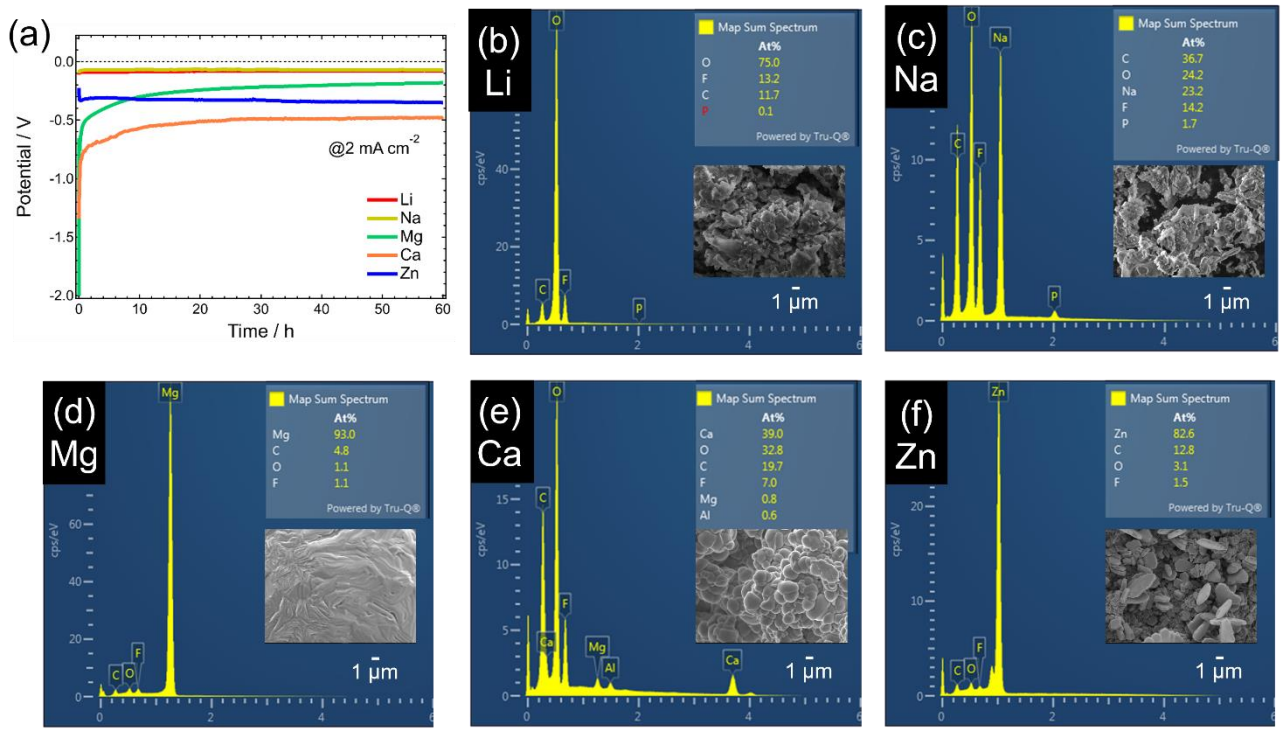

Figure 5. (a) Galvanostatic polarization curves at a current density of 2 mA cm^{-2} in 0.5 mol dm^{-3} M(I)[B(HFIP)$_4$]/G1 and 0.25 mol dm^{-3} M(II)[B(HFIP)$_4$]$_2$/G1 electrolytes. The SEM images and corresponding EDX spectra of the obtained deposits from the (b) Li-, (c) Na-, (d) Mg-, (e) Ca-, and (f) Zn-based electrolytes.

Among the studied monovalent and divalent systems, remarkably favorable efficiency was observed for Mg[B(HFIP)$_4$]$_2$/G1. The suppressed side reactions during deposition-dissolution in the electrolyte were also evidenced by SEM observations and subsequent EDX analysis of the deposits. Highly pure macrocrystalline magnesium metal could indeed be deposited, whereas mumbled deposits containing large amounts of C, F, and O atoms attributable to the decomposition products of the electrolytes were observed in the M(I)[B(HFIP)$_4$]/G1 systems. The substantially small overpotential for M(I)[B(HFIP)$_4$]/G1 suggests chemical instability of the electrolyte components against the deposited alkali metals. Regarding the chemical composition of the deposits obtained from Ca[B(HFIP)$_4$]$_2$/G1 and

$Zn[B(HFIP)_4]_2$/G1, although the elements attributable to both solvent G1 (C and O) and $[B(HFIP)_4]^-$ anion (F) were detected, the solvent decomposition seems to have taken placed preferentially. The C 1s, O 1s, F 1s, and B 1s spectra of the deposits showed similar spectral features irrespective of metal species, as the peaks assignable to oxide, hydroxide, carbonate, fluoride, and species containing C=O, C-O, and CF_n appeared in all samples (Figure S8), while the relative and absolute peak intensities strongly depend on the metal species. These elemental analysis on the deposits strongly suggest that the $M(II)[B(HFIP)_4]_2$ salts are well dissociated in solution, and highly polarized G1 molecules bound to divalent cations are decomposed by freshly deposited metals. The large crystal size of Mg deposits also suggests suppressed electrolyte decomposition and favorable nucleus-growth mode during deposition owing to the mild polarization behavior.[62] As the solution state of $Mg[B(HFIP)_4]_2$/G1 should be the same as those of $Ca[B(HFIP)_4]_2$/G1 and $Zn[B(HFIP)_4]_2$/G1, the modest surface reactivity of the deposited macrocrystalline Mg, moderate reductive nature of Mg metal, and well-balanced mutual interactions among Mg^{2+}-$[B(HFIP)_4]$-solvent may jointly contribute to the outstanding performance. The relatively large decomposition barrier of $[B(HFIP)_4]^-$ for Mg^+-$[B(HFIP)_4]^-$ ion pair compared to that for Ca^+-$[B(HFIP)_4]^-$ ion pair also partly corroborates the satisfactorily high stability of the $Mg[B(HFIP)_4]_2$/G1 electrolyte at the [electrolyte | electrode] interface.[43] The recent comprehensive work on Li metal battery electrolytes also emphasizes that diminishing electrolyte decomposition is essential to achieve high Coulombic efficiency for metal deposition/dissolution cycling.[4]

In addition to the intrinsic stability of the electrolyte components against metal electrodes, the reaction products at the [electrode | electrolyte] interface, the so-called solid electrolyte interface (SEI), play a dominant role in electrochemical reactions. The construction of a “good” SEI is crucial to achieve stable cycling of metal electrodes, and the studies on the interfacial engineering indeed attract significant attentions particularly in recent years. A family

of fluorosulfonyl amide (or imides), such as bis(fluorosulfonyl)amide ($[FSA]^-$), anions is regarded as definitive generators for "good" SEI, irrespective of the cation species except for Mg.[3,4,63–65] The decomposition products derived primarily from these anions effectively suppress the undesired intermittent reactions between electrolytes and electrodes, and further promote interfacial kinetics. Such favorable interface allows application of electrolytes even those composed of the thermodynamically unstable components against reductive metals.[66,67] However, as shown in Figures 5 and Figure S8, the interface derived from the decomposition of $[B(HFIP)_4]^-$ seems unstable and continuous electrolyte decomposition took place especially for highly reductive Li, Na, and Ca systems. As the $[B(HFIP)_4]$-derived interfaces are composed of C, F, and O atoms, whereas the [(T)FSA]-derived interfaces generally contain C, F, O, and S atoms, S-based compounds would significantly contribute to stabilizing the [electrode | electrolyte] interface. The stable cycling of rechargeable metal-sulfur batteries incorporating fluorinated alkoxyborate and alkoxyaluminate families supports favorable interface formation by sulfur species.[40,41,68]

Conclusions

In this work, inspired by the recent success stories of the $[B(HFIP)_4]^-$ based monovalent and divalent electrolytes in various battery applications, the effect of the valency of cation species on the molecular structure of the salts, and transport and electrochemical characteristics of the electrolyte solutions were studied comprehensively to gain fundamental understanding of the characteristics of this anion. X-ray crystallography revealed the formation of adducts or solvates with the solvent G1 molecule(s), irrespective of the valency of the cation species, whereas the dissociation states of the salts were dependent on the valency of the cation species. The substantially large contribution of induction interactions to the stability of divalent

solvates was found responsible for the fully isolated ion-pair formation in the solid state. The transport properties of the electrolyte solutions were found to reflect such differences in the dissociativity even in the solution states, as all divalent electrolytes exhibited greater conductivities than their monovalent counterparts despite the comparable viscosity and net number of charged species present in each solution. The analysis based on Walden plots supported the relative dissociative nature of the divalent salts.

Comparative electrochemical studies provided insights into $[B(HFIP)_4]$-based electrolyte solutions. The dissociation of the salts predominated the interfacial reaction kinetics as reversible metal deposition-dissolution with negligible overpotential were achieved for the relatively associative monovalent systems, while substantially large overpotentials, especially for the deposition processes, were required for the dissociative divalent counterparts. The substantially large desolvation barrier for the [M(II)·3(G1)] complexes due to the strong induction interactions between divalent cations and the polarized G1 molecules is responsible for these results. Further, the non-trivial oxyphilic nature of Zn(II) imparted an unexpectedly inferior electrochemical performance for dissolution processes. Contrary to the sufficient reductive stability observed for the isolated anion, results from the morphological and elemental analyses of the deposits revealed instability of the anion at the interface. Among the studied $[B(HFIP)_4]$-based mono- and divalent electrolytes, those containing Mg(II) exhibit the most remarkable electrochemical properties. These performances can further be improved by combining the $Mg[B(HFIP)_4]_2$ salt with G2,[32] whereas such approaches do not work well for the other systems (Figure S9), suggesting a certain "magic combination" of $Mg[B(HFIP)_4]_2$ and glyme solvents. The moderately reductive nature of Mg metal and the well-balanced Mg(II)–$[B(HFIP)_4]$–glyme interactions are responsible for this specific combination.

It should be noted that the interfacial stability and resulting electrochemical metal deposition/dissolution characteristics strongly depend on the composition of electrolytes and

electrodes used for the experiments. Certain fluorinated alkoxyborate and alkoxyaluminate-based electrolytes indeed showed favorable compatibility against various promising negative and positive electrode materials upon appropriate compositional and interfacial engineering.[40,41] The $Mg[B(HFIP)_4]_2$-based electrolytes also exhibit improved interfacial characteristics when favorable interfaces are constructed by adding specific agents in the electrolyte solutions.[69,70] Although further detailed understanding and optimal interfacial engineering are required to maximize the benefits of the $[B(HFIP)_4]$-based electrolytes, the remarkable ion transport characteristics and excellent oxidative stabilities allow them to be selected as the first option for next-generation energy storage applications utilizing various metal negative electrodes.

CRediT authorship contribution statement

Toshihiko Mandai: Conceptualization, Data curation, formal analysis, funding acquisition, Investigation, Project administration, Resources, Validation, Writing the original draft, review, and editing. Hiroko Naya: Data curation and validation. Hyuma Masu: Formal analysis, writing, review, and editing.

Conflict of Interests

There is no conflict of interest to declare.

Supporting Information

Crystallographic data of $Li[B(HFIP)_4]\cdot G1$, $Na[B(HFIP)_4]\cdot G1$, $Ca[B(HFIP)_4]_2\cdot 4G1$, and $Zn[B(HFIP)_4]_2\cdot 3G1$ (Table 1); thermal ellipsoid models of $Li[B(HFIP)_4]\cdot G1$ (Figure S1)

and Na[B(HFIP)$_4$]·G1 (Figure S2); ^{1}H NMR spectra of the [B(HFIP)$_4$]-based salts (Figure S3); temperature and concentration-dependent ionic conductivities of Li[B(HFIP)$_4$]/G1, Na[B(HFIP)$_4$]/G1, and Zn[B(HFIP)$_4$]$_2$/G1 (Figure S4); transport properties of [TFSA]-based mono- and divalent solutions measured at 30 °C (Figure S5); cyclic voltammograms of Pt working electrodes recorded in 0.25 mol dm^{-3} Zn[B(HFIP)$_4$]$_2$ dissolved in acetonitrile, propylene carbonate, and dimethylformamide (Figure S6); Raman spectra of the [B(HFIP)$_4$]-based salts and their G1 solutions (Figure S7); XPS spectra of the deposited metals (Figure S8); cyclic voltammograms recorded in 0.5 mol dm^{-3} Li[B(HFIP)$_4$]/G*n* and 0.25 mol dm^{-3} Zn[B(HFIP)$_4$]$_2$/G*n* (*n* = 1 or 2) (Figure S9).

Acknowledgments

This work was financially supported by the NEXT Center of Innovation Program (COI-NEXT, Grant Number JPMJPF2016) of the Japan Science and Technology Agency (JST), a Grant-in-Aid for Scientific Research (KAKENHI, Grant Number 21K05263) of the Japan Society for the Promotion of Science (JSPS), and a Research Grant for Young Researchers of the Electrochemical Society of Japan (ECSJ). The authors are also grateful for the kind support provided at the NIMS Battery Research Platform for SEM observations.

References

1. Zhang, H.; Qiao, L.; Kühnle, H.; Figgemeier, E.; Armand, M.; Eshetu, G. G. From lithium to emerging mono- and multivalent cation-based rechargeable batteries: non-aqueous organic electrolyte and interphase perspectives. *Energy Environ. Sci*. **2023**, *16*, 11−52.

2. Ghazi, Z. A.; Sun, Z.; Sun, C.; Qi, F.; An, B.; Li, F.; Cheng, H.-M. Key Aspects of Lithium Metal Anodes for Lithium Metal Batteries. *Small* **2019**, *15*, 1900687.
3. Tikekar, M. D.; Choudhury, S.; Tu, Z.; Archer, L. A. Design principles for electrolytes and interfaces for stable lithium-metal batteries. *Nat. Energy*, **2016**, *1*, 16114.
4. Ko, S.; Obukata, T.; Shimada, T.; Takenaka, N.; Nakayama, M.; Yamada, A.; Yamada, Y. Electrode potential influences the reversibility of lithium-metal anodes. *Nat. Energy* **2022**, *7*, 1217−1224.
5. Liu, Y.; Ju, Z.; Zhang, B.; Wang, Y.; Nai, J.; Liu, T.; Tao, X. Visualizing the Sensitive Lithium with Atomic Precision: Cryogenic Electron Microscopy for Batteries. *Acc. Chem. Res*. **2021**, *54*, 2088−2099
6. Vishnugopi, B. S.; Hao, F.; Verma, A.; Mukherjee, P. P. Double-Edged Effect of Temperature on Lithium Dendrites. *ACS Appl. Mater. Interfaces* **2020**, *12*, 23931−23938.
7. Sun, B.; Xiong, P.; Maitra, U.; Langsdorf, D.; Yan, K.; Wang, C.; Janek, J.; Schröder, D.; Wang, G. Design Strategies to Enable the Efficient Use of Sodium Metal Anodes in High-Energy Batteries. *Adv. Mater*. **2020**, *32*, 1903891.
8. Liu, F.; Cao, G.; Ban, J.; Lei, H.; Zhang, Y.; Shao, G.; Zhou, A.; Fan, L.; Hu, J. Recent advances based on Mg anodes and their interfacial modulation in Mg batteries. *J. Magnesium Alloys* **2022**, *10*, 2699-2716.
9. Dompablo, M. E. A.; Ponrouch, A.; Johansson, P.; Palacín, M. R. *Chem. Rev.* **2020**, *120*, 6331-6357.
10. Zhang, T.; Tang, Y.; Guo, S.; Cao, X.; Pan, A.; Fang, G.; Zhou, J.; Liang, S. Fundamentals and perspectives in developing zinc-ion battery electrolytes: a comprehensive review. *Energy Environ. Sci*. **2020**, *13*, 4625-4665.
11. Zhang, H.; Qiao, L.; Armand, M. Organic Electrolyte Design for Rechargeable Batteries: From Lithium to Magnesium. *Angew. Chem. Int. Ed*. **2022**, *61*, e202214054.
12. Huang, M.; Feng, S.; Zhang, W.; Giordano, L.; Chen, M.; Amanchukwu, C. V.; Anandakathir, R.; Horn, Y. S.; Johnson, J. A. Fluorinated Aryl Sulfonimide Tagged (FAST) salts: modular synthesis and structure–property relationships for battery applications. *Energy Environ. Sci*. **2018**, *11*, 1326−1334.
13. Nishikawa, K.; Shinoda, K.; Kanamura, K. 3D Structural Transition of the Electrodeposited and Electrochemically Dissolved Li Metal onto an Ultramicroelectrode. *J. Phys. Chem. C* **2020**, *124*, 22019–22024.
14. Li, X.; Zheng, J.; Engelhard, m. H.; Mei, D.; Li, Q.; Jiao, S.; Liu, N.; Zhao, W.; Zhang, J.-G.; Xu, W. Effects of Imide−Orthoborate Dual-Salt Mixtures in Organic Carbonate Electrolytes on the Stability of Lithium Metal Batteries. *ACS Appl. Mater. Interfaces* **2018**, *10*, 2469−2479

15. Wang, Q.; Zhao, C.; Lv, X.; Lu, Y.; Lin, K.; Zhang, S.; Kang, F.; Hu, Y.-S.; Li, B. Stabilizing a sodium-metal battery with the synergy effects of a sodiophilic matrix and fluorine-rich interface. *J. Mater. Chem. A* **2019**, *7*, 24857–24867
16. Lee, Y.; Lee, J.; Lee, J.; Kim, K.; Cha, A.; Kang, S.; Wi, T.; Kang, S. J.; Lee, H.-W.; Choi, N.-S. Fluoroethylene Carbonate-Based Electrolyte with 1 M Sodium Bis(fluorosulfonyl)imide Enables High-Performance Sodium Metal Electrodes. *ACS Appl. Mater. Interfaces* **2018**, *10*, 15270−15280
17. Lu, Z.; Schechter, A.; Moshkovich, M.; Aurbach, D. On the electrochemical behavior of magnesium electrodes in polar aprotic electrolyte solutions. *J. Electroanal. Chem*. **1999**, *466*, 203–217.
18. Hayashi, M.; Arai, H.; Ohtsuka, H.; Sakurai, Y. Electrochemical characteristics of calcium in organic electrolyte solutions and vanadium oxides as calcium hosts. *J. Power Sources* **2003**, *119*, 617–620.
19. J. Barthel, M. Wu:hr, R. Buestrich, and H. J. Gores. A New Class of Electrochemically and Thermally Stable Lithium Salts for Lithium Battery Electrolytes I. Synthesis and Properties of Lithium bis[1,2-benzenediolato(2-)-O,O']borate. *J. Electrochem. Soc*. **1995**, *142*, 2527−2531
20. J. Barthel, R. Buesfrich, E. Carl, and H. J. Gore. A New Class of Electrochemically and Thermally Stable Lithium Salts for Lithium Battery Electrolytes II. Conductivity of Lithium Organoborates in Dimethoxyethane and Propylene Carbonate. *J. Electrochem. Soc*. **1996**, *143*, 3565−3571.
21. J. Barthel, R. Buestrich, E. Cad, and H. J. Gore. A New Class of Electrochemically and Thermally Stable Lithium Salts for Lithium Battery Electrolytes Ill. Synthesis and Properties of Some Lithium Organoborates. *J. Electrochem. Soc*. **1996**, *143*, 3572−3575.
22. J. Barthel, R. Buestrich, H. J. Gores, M. Schmidt, and M. Wuhr. A New Class of Electrochemically and Thermally Stable Lithium Salts for Lithium Battery Electrolytes IV. Investigations of the Electrochemical Oxidation of Lithium Organoborates. *J. Electrochem. Soc*. **1997**, *144*, 3866−3870.
23. J. Barthel, M. Schmidt, and H. J. Gores. Lithium Bis[5-fluoro-2-olato-1-benzenesulfonato(2-)-O,O']borate, a New Anodically and Cathodically Stable Salt for Electrolytes of Lithium-Ion Cells. *Electrochem. Soc. Lett*. **1998**, *145*, L17−L20.
24. Tsujioka, S.; Nolan, B. G.; Takase, H.; Fauber, B. P.; Strauss, S. H. Conductivities and Electrochemical Stabilities of Lithium Salts of Polyfluoroalkoxyaluminate Superweak Anions. *J. Electrochem. Soc.* **2004**, *151*, A1418.
25. Xu, W.; Angell, C. A. A Fusible Orthoborate Lithium Salt with High Conductivity in Solutions. *Electrochem. Solid State Lett*. **2000**, *3*, 366-368.
26. Ivanova, S. M.; Nolan, B. G.; Kobayashi, Y.; Miller, S. M.; Anderson, O. P.; Strauss, S. H. Relative Lewis Basicities of Six $Al(OR^F)_4^-$ Superweak Anions and the Structures of

LiAl{OCH(CF_3)$_2$}$_4$ and [1-Et-3-Me-1,3-$C_3H_3N_2$][Li{Al{OCH(CF_3)$_2$}$_4$}$_2$]. *Chem. Eur. J.* **2001**, *7*, 503–510.

27. Krossing, I.; Raabe, I. Noncoordinating Anions—Fact or Fiction? A Survey of Likely Candidates. *Angew. Chem. Int. Ed*. **2004**, *43*, 2066–2090.
28. Karger, Z. Z.; Bardaji, M. E. G.; Fuhr, O.; Fichtner, M. A new class of non-corrosive, highly efficient electrolytes for rechargeable magnesium batteries. *J. Mater. Chem. A* **2017**, *5*, 10815–10820.
29. Mandai, T. Critical Issues of Fluorinated Alkoxyborate–Based Electrolytes in Magnesium Battery Applications. *ACS Appl. Mater. Interface* **2020**, *12*, 39135–39144.
30. Zhao-Kerger, Z.; Liu, R.; Dai, W.; Li, Z.; Diemant, T.; Vinayan, B. P.; Minella, C. B.; Yu, X.; Manthiram, A.; Behm, R. J. et al. Toward Highly Reversible Magnesium−Sulfur Batteries with Efficient and Practical Mg[B(hfip)$_4$]$_2$ Electrolyte. *ACS Energy Lett*. **2018**, *3*, 2005–2013.
31. Herb, J. T.; Nist-Lund, C. A.; Arnold, C. B. A Fluorinated Alkoxyaluminate Electrolyte for Magnesium-Ion Batteries. *ACS Energy Lett*. **2016**, *1*, 1227–1232.
32. Mandai, T.; Youn, Y.; Tateyama, Y. Remarkable electrochemical and ion-transport characteristics of magnesium-fluorinated alkoxyaluminate–diglyme electrolytes for magnesium batteries. *Mater. Adv*. **2021**, *2*, 6283–6296.
33. Pavčnik, T.; Lozinšek, M.; Pirnat, K.; Vizintin, A.; Mandai, T.; Aurbach, D.; Dominko, R.; Bitenc, J. On the Practical Applications of the Magnesium Fluorinated Alkoxyaluminate Electrolyte in Mg Battery Cells. *ACS Appl. Mater. Interfaces* **2022**, *14*, 26766−26774.
34. Lau, K.-C.; Seguin, T. J.; Carino, E. V.; Hahn, N. T.; Connell, J. G.; Ingram, B. J.; Persson, K. A.; Zavadil, K. R.; Liao, C. Widening Electrochemical Window of Mg Salt by Weakly Coordinating Perfluoroalkoxyaluminate Anion for Mg Battery Electrolyte. *J. Electrochem. Soc*. **2019**, *166*, A1510-A1519.
35. Li, Z.; Fuhr, O.; Fichtner, M.; Karger, Z. Z. Towards stable and efficient electrolytes for room-temperature rechargeable calcium batteries. *Energy Environ. Sci*. **2019**, *12*, 3496-3501
36. Shyamsunder, A.; Blanc, L. E.; Assoud, A.; Nazar, L. F. Reversible Calcium Plating and Stripping at Room Temperature Using a Borate Salt. *ACS Energy Lett*. **2019**, *4*, 2271–2276.
37. Yang, M.; Driscoll, D. M.; Balasubramanian, M.; Liao, C. Solvation Structure and Electrochemical Properties of a New Weakly Coordinating Aluminate Salt as a Nonaqueous Electrolyte for Zinc Batteries. *J. Electrochem. Soc*. **2020**, *167*, 160529.
38. Roy, B.; Cherepanov, P.; Nguyen, C.; Forsyth, C.; Pal, U.; Mendes, T. C.; Howlett, P.; Forsyth, M.; MacFarlane, D.; Kar, M. Lithium Borate Ester Salts for Electrolyte Application in Next-Generation High Voltage Lithium Batteries. *Adv. Energy Mater*. **2021**, *11*, 2101422.
39. Ould, D. M. C.; Menkin, S.; Smith, H. E.; Gonzalez, V. R.; Jónsson,E.; O'Keefe, C. A.; Coowar, F.; Barker, J.; Bond, A. D.; Grey, C. P. et al. Sodium Borates: Expanding the

Electrolyte Selection for Sodium-Ion Batteries. *Angew. Chem. Int. Ed*. **2022**, *61*, e202202133.

40. Murugan, S.; Klostermann, S. V.; Frey, W.; Kästner, J.; Buchmeiser, M. R. A sodium bis(perfluoropinacol) borate-based electrolyte for stable, high-performance room temperature sodium-sulfur batteries based on sulfurized poly(acrylonitrile). *Electrochem. Commun*. **2021**, *132*, 107137.
41. Shyamsunder, A.; Beichel, W.; Klose, P.; Pang, Q.; Scherer, H.; Hoffmann, A.; Murphy, G. K.; Krossing, I.; Nazar, L. F. Inhibiting Polysulfide Shuttle in Lithium–Sulfur Batteries through Low-Ion-Pairing Salts and a Triflamide Solvent. *Angew. Chem. Int. Ed*. **2017**, *56*, 6192 –6197.
42. Jankowski, P.; Li, Z.; Karger, Z. Z.; Diemant, T.; Fichtner, M.; Vegge, T.; Lastra, J. M. G. Development of Magnesium Borate Electrolytes: Explaining the Success of $Mg[B(hfip)_4]_2$ Salt. *Energy Storage Mater*. **2022**, *45*, 1133–1143.
43. Xie, X.; Leon, N. J.; Small, D. W.; Smith, E. W. C. S.; Liao, C.; Persson, K. A. Reductive Decomposition Kinetics and Thermodynamics That Govern the Design of Fluorinated Alkoxyaluminate/Borate Salts for Mg-Ion and Ca-Ion Batteries. *J. Phys. Chem. C* **2022**, *126*, 20773−20785.
44. Zhang, S.; Cheng, M.; Zhang, P.; Wang, Y.; Zhang, D.; Yang, Y.; Wang, J.; NuLi, Y. Insights into the stability of magnesium borate salts for rechargeable magnesium batteries from AIMD simulations. *Chem. Commun*. **2022**, *58*, 11969–11972.
45. Bulut, S.; Klose, P.; Krossing, I. $Na[B(hfip)_4]$ (hfip = $OC(H)(CF_3)_2$): a weakly coordinating anion salt and its first application to prepare ionic liquids. *Dalton Trans.* **2011**, *40*, 8114–8124.
46. Nakayama, K. Guidance for the Vacuum Engineer Examination (4). *J. Vac. Soc. Jpn*. **2011**, *54*, 458−459
47. Tsuzuki, S.; Shinoda, W.; Seki, S.; Umebayashi, Y.; Yoshida, K.; Dokko, K.; Watanabe, M. Intermolecular Interactions in Li^+-glyme and Li^+-glyme–TFSA− Complexes: Relationship with Physicochemical Properties of [Li(glyme)][TFSA] Ionic Liquids. *ChemPhysChem* **2013**, *14*, 1993−2001.
48. Tsuzuki, S.; Mandai, T.; Suzuki, S.; Shinoda, W.; Nakamura, T.; Morishita, T.; Ueno, K.; Seki, S.; Umebayashi, Y.; Dokko, K. et al. Effect of the cation on the stability of cation–glyme complexes and their interactions with the $[TFSA]^-$ anion. *Phys. Chem. Chem. Phys*. **2017**, *19,* 18262−18272.
49. Keyzer, E. N.; Glass, H. F. J.; Liu, Z.; Bayley, P. M.; Dutton, S. E.; Grey, C. P.; Wright, D. S. $Mg(PF_6)_2$-Based Electrolyte Systems: Understanding Electrolyte−Electrode Interactions for the Development of Mg-Ion Batteries. *J. Am. Chem. Soc*. **2016**, *138*, 8682−8685.

50. Laoire, C. O.; Mukerjee, S.; Abraham, K. M.; Plichta, E. J.; Hendrickson, M. A. Influence of Nonaqueous Solvents on the Electrochemistry of Oxygen in the Rechargeable Lithium−Air battery. *J. Phys. Chem. C* **2010**, *114*, 9178−9186.
51. Yu, X.; Boyer, M. J.; Hwang, G. S.; Manthiram, A. Toward a Reversible Calcium-Sulfur Battery with a Lithium-Ion Mediation Approach. *Adv. Energy Mater*. **2019**, *9*, 1803794.
52. Horwitz, G.; Factorovich, M.; Rodriguez, J.; Laria, D.; Corti, H. R. Ionic Transport and Speciation of Lithium Salts in Glymes: Experimental and Theoretical Results for Electrolytes of Interest for Lithium−Air Batteries. *ACS Omega* **2018**, *3*, 11205−11215.
53. Salama, M.; Shterenberg, I.; Gizbar, H.; Eliaz, N. N.; Kosa, M.; Adamsky, K. K.; Afri, M.; Shimon, L. J. W.; Gottlieb, H. E.; Major, D. T.; Gofer, Y.; Aurbach, D. Unique Behavior of Dimethoxyethane (DME)/$Mg(N(SO_2CF_3)_2)_2$ Solutions. *J. Phys. Chem. C* **2016**, *120*, 19586−19594
54. Mandai, T.; Yoshida, K.; Tsuzuki, S.; Nozawa, R.; Masu, H.; Ueno, K.; Dokko, K.; Watanabe, M. Effect of Ionic Size on Solvate Stability of Glyme-Based Solvate Ionic Liquids. *J. Phys. Chem. B* **2015**, *119*, 1523−1534.
55. Tutusaus, O.; Mohtadi, R.; Arthur, T. S.; Mizuno, F.; Nelson, E. G.; Sevryugina, Y. V. An Efficient Halogen-Free Electrolyte for Use in Rechargeable Magnesium Batteries. *Angew. Chem. Int. Ed*. **2015**, *54*, 7900–7904.
56. Yoshida, K.; Nakamura, M.; Kazue, Y.; Tachikawa, N.; Tsuzuki, S.; Seki, S.; Dokko, K.; Watanabe, M. Oxidative-Stability Enhancement and Charge Transport Mechanism in Glyme–Lithium Salt Equimolar Complexes. *J. Am. Chem. Soc*. **2011**, *133*, 13121–13129.
57. Shimokawa, K.; Matsumoto, H.; Ichitsubo, T. Solvation-Structure Modification by Concentrating $Mg(TFSA)_2$−$MgCl_2$−Triglyme Ternary Electrolyte. *J. Phys. Chem. Lett*. **2018**, *9*, 4732−4737.
58. Han, S.-D.; Rajput, N. N.; Qu, X.; Pan, B.; He, M.; Ferrandon, M. S.; Liao, C.; Persson, K. A.; Burrell, A. K. Origin of Electrochemical, Structural, and Transport Properties in Nonaqueous Zinc Electrolytes. *ACS Appl. Mater. Interfaces* **2016**, *8*, 3021−3031.
59. University of Cambridge. The Ellingham diagram in removal of contaminants. Dissemination of IT for the Promotion of Materials Science (DoITPoMS), TLP Library. https://www.doitpoms.ac.uk/tlplib/recycling-metals/ellingham.php (accessed February 16th, 2023).
60. Bitenc, J.; Scafuri, A.; Pirnat, K.; Lozinšek, M.; Jerman, I.; Grdadolnik, J.; Fraisse, B.; Berthelot, R.; Stievano, L.; Dominko, R. Electrochemical Performance and Mechanism of Calcium Metal-Organic Battery. *Batteries & Supercaps* **2021**, *4*, 214−220.
61. Zheng, J.; Zhao, Q.; Tang, T.; Yin, J.; Quilty, C. D.; Renderos, G. D.; Liu, X.; Deng, Y.; Wang, L.; Bock, D. C. et al. Reversible epitaxial electrodeposition of metals in battery anodes. *Science*, **2019**, *366*, 645–648.

62. Davidson, R.; Verma, A.; Santos, D.; Hao, F.; Fincher, C. D.; Zhao, D.; Attari, V.; Schofield, P.; Buskirk, J. V.; Cartagena, A. F. et al. Mapping mechanisms and growth regimes of magnesium electrodeposition at high current densities. *Mater. Horiz*., **2020**, *7*, 843–854.
63. Lee, J.; Lee, Y.; Lee, J.; Lee, S.-M.; Choi, J.-H.; Kim, H.; Kwon, M.-S.; Kang, K.; Lee, K. T.; Choi, N. S. Ultraconcentrated Sodium Bis(fluorosulfonyl)imide-Based Electrolytes for High-Performance Sodium Metal Batteries. *ACS Appl. Mater. Interfaces* **2017**, *9*, 3723−3732.
64. Li, J.; Han, C.; Ou, X.; Tang, Y. Concentrated Electrolyte for High-Performance Ca-Ion Battery Based on Organic Anode and Graphite Cathode. *Angew. Chem. Ind. Ed*. **2022**, *61*, e202116668
65. Mandai, T.; Tatesaka, K.; Soh, K.; Masu, H.; Choudhary, A.; Tateyama, Y.; Ise, R.; Imai, H.; Takeguchi, T.; Kanamura, K. Modifications in coordination structure of Mg[TFSA]$_2$-based supporting salts for high-voltage magnesium rechargeable batteries. *Phys. Chem. Chem. Phys*. **2019**, *21*, 12100–12111.
66. Yamada, Y.; Furukawa, K.; Sodeyama, K.; Kikuchi, K.; Yaegashi, M.; Tateyama, Y.; Yamada, A. Unusual Stability of Acetonitrile-Based Superconcentrated Electrolytes for Fast-Charging Lithium-Ion Batteries. *J. Am. Chem. Soc*. **2014**, *136*, 13, 5039–5046.
67. Tatara, R.; Nishimura, S.; Okamoto, Y.; Ueno, K.; Watanabe, M.; Dokko, K. Structures and Electrochemistry of γ-Butyrolactone Solvates of Na Salts. *J. Phys. Chem. C* **2020,** *124*, 15800−15811.
68. Li, Z.; Vinayan, B. P.; Diemant, T.; Behm, R. J.; Fichtner, M.; Karger, Z. Z. Rechargeable Calcium–Sulfur Batteries Enabled by an Efficient Borate-Based Electrolyte. *Small* **2020**, *16*, 2001806
69. Tang, K.; Du, A.; Dong, S.; Cui, Z.; Liu, X.; Lu, C.; Zhao, J.; Zhou, X.; Cui, G. A Stable Solid Electrolyte Interphase for Magnesium Metal Anode Evolved from a Bulky Anion Lithium Salt. *Adv. Mater*. **2020**, *32*, 1904987.
70. Meng, Z.; Li, Z.; Wang, L.; Diemant, T.; Bosubabu, D.; Tang, Y.; Berthelot, R.; Karger, Z. Z.; Fichtner, M. Surface Engineering of a Mg Electrode via a New Additive to Reduce Overpotential. *ACS Appl. Mater. Interfaces* **2021**, *13*, 37044−37051.

TOC Graphic

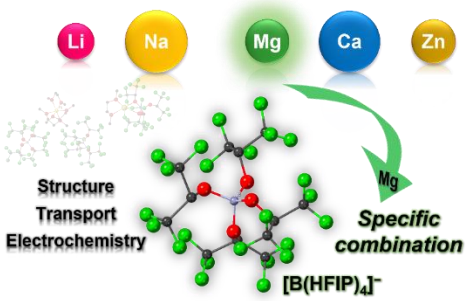
Li
Na
Mg
Ca
Zn
Structure
Transport
Electrochemistry
Mg
Specific
combination
[B(HFIP)4]-